Computer Modeling in Engineering & Sciences

Tech Science Press

DOI: 10.32604/cmes.2023.044094

ARTICLE

Interaction Mechanisms between Natural Debris Flow and Rigid Barrier Deflectors: A New Perspective for Rational Design and Optimal Arrangement

Yu Huang[1], Beilei Liu[1], Dianlei Feng[2,*] and Hao Shi[1]

[1]Department of Geotechnical Engineering, College of Civil Engineering, Tongji University, Shanghai, 200092, China

[2]Department of Hydraulic Engineering, College of Civil Engineering, Tongji University, Shanghai, 200092, China

*Corresponding Author: Dianlei Feng. Email: dianleifeng@tongji.edu.cn

Received: 20 July 2023 Accepted: 31 October 2023 Published: 29 January 2024

ABSTRACT

Rigid barrier deflectors can effectively prevent overspilling landslides, and can satisfy disaster prevention requirements. However, the mechanisms of interaction between natural granular flow and rigid barrier deflectors require further investigation. To date, few studies have investigated the impact of deflectors on controlling viscous debris flows for geological disaster prevention. To investigate the effect of rigid barrier deflectors on impact mechanisms, a numerical model using the smoothed particle hydrodynamics (SPH) method with the Herschel–Bulkley model is proposed to simulate the interaction between natural viscous flow and single/dual barriers with and without deflectors. This model was validated using laboratory flume test data from the literature. Then, the model was used to investigate the influence of the deflector angle and multi-barrier arrangements. The optimal configuration of multi-barriers was analyzed with consideration to the barrier height and distance between the barriers, because these metrics have a significant impact on the viscous flow pile-up, run-up, and overflow mechanisms. The investigation considered the energy dissipation process, retention efficiency, and dead-zone formation. Compared with bare barriers with similar geometric characteristics and spatial distribution, rigid barriers with deflectors exhibit superior effectiveness in preventing the overflow and overspilling of viscous debris flow. Recommendations for the rational design of deflectors and the optimal arrangement of multi-barriers are provided to mitigate geological disasters.

KEYWORDS

Rigid barrier deflectors; deflector angle; single-barrier; dual-barrier arrangements; viscous debris flow; over-spilling; delta-plus-SPH

1 Introduction

Rigid barriers can effectively prevent natural hazards caused by mass-wasting debris flows in mountainous regions [1,2]. In large-scale natural debris flow disasters, bare barriers cannot retain flow material, and do not satisfy existing disaster protection requirements. Many design recommendations have been proposed to prevent debris flows from overflowing and overspilling [3,4]. For mitigation purposes, deflectors positioned atop the wall stem can redirect debris flows. The parapets in coastal structures are prototypes of these deflectors, and were initially designed to minimize water overspill

and splash back [5,6]. The reduction factor quantifies the effectiveness of deflectors by measuring the discharge that overtops a barrier with a deflector in place and dividing this amount by the discharge that overtops a barrier without a deflector [7]. The comparison of bare barriers and rigid barriers with deflectors is shown in detail in Fig. 1, where B_{height} is the barrier height, L is the horizontal length of deflectors, and h_{max} is the maximum approach debris thickness. Owing to the larger volume of natural debris material, it is necessary to consider the barrier height, deflector height, and angles (equal to the horizontal length L) of the deflectors at the wall crest [8]. Because the rheological behaviors of water and debris flow are different, the design of deflectors, which aim to prevent natural debris flow, should be optimized based on parapets.

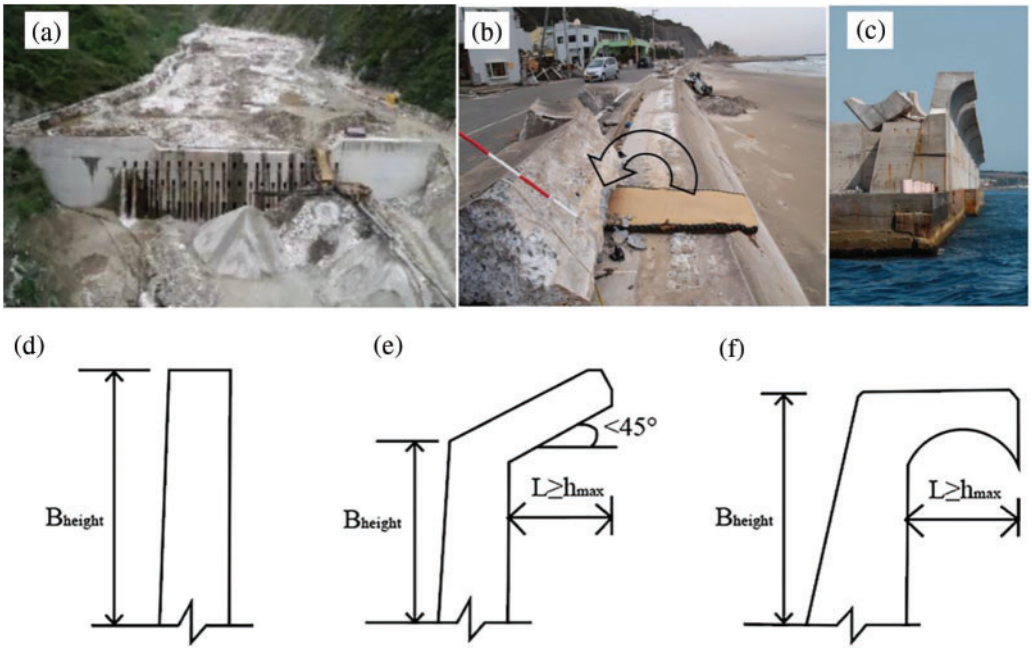

Figure 1: Countermeasures in hazard mitigation: (a) dredging of blocking structures in in the Qipan gully (China) [9]; (b) parapet failure in Toyoma Coast, Fukushima (Japan) [10]; (c) damages that occurred at Civitavecchia Port, Lazio, Italy [11]; (d) bare rigid barrier; (e) rigid barrier with inclined deflector; (f) rigid barrier with curved orthogonal deflector, modified from [8]

The interactions between debris flows and deflectors have been investigated using both physical and numerical models. Choi et al. [12] conducted preliminary small-scale flume experiments to investigate dry granular flow interaction with deflectors that had different angles. Ng et al. [4] conducted flume tests to investigate the flow kinematics of dry sand flows and the energy dissipation under the influence of deflectors. The results obtained by previous studies have revealed that conditions for adverse overflow strongly depend on the effective barrier height and length, and deflector angle. Notably, the flow characteristics of viscous debris flow differ significantly to those of dry granular flow, resulting in overspilling and hydrodynamic dead-zone formation [13–15]. Ng et al. [16] discussed the impact kinematics of fluids, including water and slurry, under different deflector geometries. A modified impact equation considering the flow-deflector interactions has been proposed. The impact, run-up, and pile-up mechanisms of saturated debris flow exhibit significant differences compared with those of dry granular flows in flow–barrier interactions. Consequently, research on the influence of deflectors on natural debris flow remains limited. Moreover, an appropriate constitutive model is

required to capture the dynamic behavior of natural debris flow accurately and elucidate the flow–deflector interaction mechanisms.

Natural debris flow, which is a typical non-Newtonian fluid, has the characteristics of shear thinning or shear thickening behavior [17]. Various non-Newtonian rheological models, such as the Bingham model [18,19], power-law model [20], and Herschel–Bulkley model [21,22], have been proposed. Moreover, the constant threshold of yield stress (τ_y) and the value of the power-law exponent (N) are key factors for changing the model in certain situations [23]. The Herschel–Bulkley fluid model has been widely used to calculate the dynamic viscosity in debris flow modeling when the power-law exponent $N \neq 1$ and yield stress $\tau_y \neq 0$. This study implemented the Herschel–Bulkley (HB) model to simulate the complex rheological behavior of debris flow and elucidate the influence of defectors on controlling viscous debris flow.

The grid-based method and particle-based method are often used for modeling flow–structure interactions. For large-deformation debris flows, mesh-free methods can avoid the grid distortion in grid-based methods. Methods such as the discrete element method (DEM) [24], coupled computational fluid dynamics and discrete element method (CFD-DEM) [25], material point method (MPM) [26], and smoothed particle hydrodynamics (SPH) [27] are typical particle-based methods for capturing the complicated flow–barrier interactions of classic geomechanical problems. Among them, the SPH method has many advantages in solving large deformation problems over traditional grid-based methods [24–26]. This method has become widespread owing to its accuracy and stability under complex boundary conditions for the quantitative analysis of the mechanisms of dynamic interaction between natural debris flows and rigid barriers [27–29]. Wang et al. [30] investigated the flow behavior of debris flows using SPH, focusing on the propagation analysis of debris flows in terms of run-out distance and flow velocity. Dai et al. [31] used SPH to investigate the interaction between debris flows and structures, and estimated the impact force. Sun et al. [32,33] proposed the particle shifting technique (PST) to maintain the numerical stability and accuracy of the δ-plus-SPH scheme. Notably, the δ-SPH scheme introduces an artificial diffusive term to improve the high-frequency noise in the pressure field. Relevant results have revealed that δ-plus-SPH is feasible and reliable for investigating the dynamic interaction between debris flows and structures.

This study developed a δ-plus-SPH method and used it to investigate the influence of deflectors on the dynamic behavior of viscous debris flow. The primary objective of this study was to investigate the influence of deflector angles on viscous debris flow in both single-barrier and dual-barrier systems. The presentation and validation of the numerical results are obtained by using the δ-plus-SPH model, followed by the discussion of energy dissipation process, retention efficiency, and run-up and overflow mechanisms of viscous debris flow in rigid barriers with and without deflectors.

2 Numerical Modeling

2.1 Numerical Method

In the domain of computational fluid dynamics, the SPH method has emerged as a prominent mesh-free Lagrangian approach [28]. Central to the SPH method is the utilization of kernel functions to compute particle interactions, ensuring both consistency and stability in the numerical representation. This subsection presents the fundamental principles and mathematical formulations of the SPH method. Each equation is systematically introduced, accompanied by a rigorous exposition of its derivation, underlying assumptions, and its role within the overarching SPH framework.

The governing equations (Eq. (1)) include the mass and momentum balance, and require numerical solutions.

$$\begin{aligned} \frac{\mathrm{d}\rho}{\mathrm{d}t} &= -\rho div\,(\boldsymbol{u}) \\ \rho\frac{\mathrm{d}\boldsymbol{u}}{\mathrm{d}t} &= -\nabla P + \nabla\cdot\boldsymbol{\tau} + \rho\boldsymbol{g} \end{aligned} \tag{1}$$

Eq. (1) has the derivative form of density and velocity; t represents time, ρ denotes the density, and $\boldsymbol{u}$ denotes the velocity. Therefore, $\frac{d\rho}{dt}$ is the time derivative of density and $\frac{d\boldsymbol{u}}{dt}$ is the time derivative of velocity. In the momentum equation, P represents pressure; $\boldsymbol{\tau}$ and $\boldsymbol{g}$ denote the deviatoric shear stress tensor and body force, respectively. In this study, the equation of state was used to calculate the pressure field. In Eq. (2), C_s is the numerical sound speed, ρ_0 represents the reference density, and P_0 denotes the background pressure.

$$P = C_s^2\left(\rho - \rho_0\right) + P_0 \tag{2}$$

Recently, the SPH method has been widely used to simulate large-deformation natural debris flows, because it can capture free surfaces and large deformable geomaterial boundaries [34]. By using the SPH method, the governing equations can be efficiently solved. The physical properties carried by the arbitrarily distributed discrete particles of debris flow are based on the distributed particles within a smoothing length. The field function $f\left(\boldsymbol{r}_i\right)$ and its derivative can be approximated as follows:

$$< f\left(\boldsymbol{r}_i\right) >= \sum_j f\left(\boldsymbol{r}_i\right)\frac{m_j}{\rho_j}W\left(\boldsymbol{r}_i - \boldsymbol{r}_j, h\right) \tag{3}$$

$$< \nabla f\left(\boldsymbol{r}_i\right) >= \sum_j f\left(\boldsymbol{r}_i\right)\nabla_i W_{ij} V_j \tag{4}$$

where $<>$ denotes the SPH approximation.

In Eqs. (3) and (4), $W\left(\boldsymbol{r}_i - \boldsymbol{r}_j, h\right)$ refers to the kernel function, and h represents the smoothing length [35]. For a given pair of particles i, j refers to adjacent particles within the supporting domain. The distance between particles i and j is $\boldsymbol{r}_{ij} = \boldsymbol{r}_i - \boldsymbol{r}_j$, where $\boldsymbol{r}_i$ denotes the position of particle i and V_j indicates the volume of a single particle. The application of the Wendland kernel function [36] in this study is expressed as follows:

$$W\left(\boldsymbol{r}_i - \boldsymbol{r}_j, h\right) = \alpha_D\left(1 - \frac{q}{2}\right)^4(2q+1) \tag{5}$$

In Eq. (5), $\alpha_D = \frac{7}{4\pi h^2}$ for two-dimensional problems, and $q = \frac{\boldsymbol{r}_{ij}}{h}$.

In this study, the particle shifting technique (PST) and δ-SPH were used to maintain the uniformity of particles and improve the pressure oscillations [37,38]. The discrete form of Eq. (1) can be expressed as follows ($\otimes$ is the Kronecker product):

$$\begin{aligned}
\frac{\mathrm{d}\rho_i}{\mathrm{d}t} &= -\rho_i \sum_j \left[\left(\boldsymbol{u}_j + \delta\boldsymbol{u}_j\right) - \left(\boldsymbol{u}_i + \delta\boldsymbol{u}_i\right)\right] \cdot \nabla_i W_{ij} V_j + \sum_{j\in\chi} \left(\rho_j \delta\boldsymbol{u}_j + \rho_i \delta\boldsymbol{u}_i\right) \cdot \nabla_i W_{ij} V_j + \delta_d h C_s \mathcal{D}_i \\
\frac{\mathrm{d}\boldsymbol{u}_i}{\mathrm{d}t} &= -\frac{1}{\rho_i} \sum_j \left(P_i + P_j\right) \nabla_i W_{ij} V_j + \frac{\rho_0}{\rho_i} \alpha \sum_j \frac{2\eta_i \eta_j}{\eta_i + \eta_j} \frac{\left(\boldsymbol{r}_i - \boldsymbol{r}_j\right) \cdot \nabla W_{ij} V_j}{r_{ij}^2} \left(\boldsymbol{u}_i - \boldsymbol{u}_j\right) \\
&\quad + \sum_j \left(\boldsymbol{u}_j \otimes \delta\boldsymbol{u}_j + \boldsymbol{u}_i \otimes \delta\boldsymbol{u}_i\right) \cdot \nabla_i W_{ij} V_j - \boldsymbol{u}_i \sum_j \left(\delta\boldsymbol{u}_j - \delta\boldsymbol{u}_i\right) \cdot \nabla_i W_{ij} V_j + \boldsymbol{g} \\
\frac{\mathrm{d}\boldsymbol{r}_i}{\mathrm{d}t} &= \boldsymbol{u}_i + \delta\boldsymbol{u}_i
\end{aligned} \tag{6}$$

In two-dimensional problems, the coefficient of the viscous term $\alpha = 8$ [39], and it is recommended that the diffusion coefficient δ is set to 0.1. The diffusion term D_i is introduced in Eq. (7) to remove the pressure noise [40].

$$D_i = \sum_j \left[2\left(\rho_i - \rho_j\right) - \left(\nabla\left(\rho\right)_i^L + \nabla\left(\rho\right)_j^L\right) \cdot \left(\boldsymbol{r}_j - \boldsymbol{r}_i\right)\right] \frac{\boldsymbol{r}_j - \boldsymbol{r}_i}{\boldsymbol{r}_{ij}} V_j \tag{7}$$

where $\nabla\left(\rho\right)_i^L$ is the density gradient in Eq. (7), which is computed using the renormalized gradient form and expressed as follows:

$$\begin{aligned}
\nabla\left(\rho\right)_i^L &= \sum_j (\rho_j - \rho_i) \boldsymbol{L}_i \cdot \nabla_i W_{ij} V_j \\
\boldsymbol{L}_i &= \left[\sum_j (\boldsymbol{r}_j - \boldsymbol{r}_i) \otimes \nabla_i W_{ij} V_j\right]^{-1}
\end{aligned} \tag{8}$$

The PST method is used to avoid arbitrary particle configuration, and the shifting velocity $\delta\overline{\boldsymbol{u}}_i$ is calculated [32] as follows:

$$\delta\overline{\boldsymbol{u}}_i = -2hu_{max} \sum \left[1 + R\left(\frac{W_{ij}}{W\left(\Delta x\right)}\right)^n\right] \nabla_i W_{ij} V_j \tag{9}$$

In Eq. (9), $u_{\max}$ represents the maximum velocity; Δx_i refers to the initial particle distance; R and n are equal to 0.2 and 4, respectively [39]. The velocity deviation $\delta\boldsymbol{u}_i$ is calculated to avoid large inconsistent kinematic boundary conditions [41].

$$\delta\boldsymbol{u}_i = \begin{cases} 0 & \text{if } \lambda_i < 0.55, \\ \left(\boldsymbol{I} - \boldsymbol{n}_i \otimes \boldsymbol{n}_i\right) \delta\boldsymbol{u}_i^* & \text{if } 0.55 \le \lambda_i \le 0.9 \text{ and } \delta\boldsymbol{u}_i^* \cdot \boldsymbol{n}_i \ge 0, \\ \delta\boldsymbol{u}_i^* & \text{else.} \end{cases} \tag{10}$$

$$\boldsymbol{u}^* = \min\left(\left\|\delta\overline{\boldsymbol{u}}_i\right\|, \frac{u_{max}}{2}\right) \frac{\delta\overline{\boldsymbol{u}}_i}{\left\|\delta\overline{\boldsymbol{u}}_i\right\|} \tag{11}$$

In Eq. (11), λ_i denotes the minimum eigenvalue of the tensor; $\boldsymbol{B}_i = \left[\sum \left(\boldsymbol{r}_j – \boldsymbol{r}_i\right) \otimes \nabla_i W_{ij} V_j\right]$; n_i refers to the vector perpendicular to the free surface of particle i [26].

This study employed the generalized wall boundary method and 4th-order Runge–Kutta time-integration technique to model intricate geometries. Notably, dummy particles can be used to model the interactions between the fluid phase and a solid boundary [42].

2.2 Numerical Model Setup and Rheological Model

Because deflectors are an efficient debris flow deflection method, a previous study [12] conducted flume tests to investigate the influence of different rigid barrier deflector angles. The overflow mechanisms are characterized by viscous flow launching off ramp-like dead zones, launch length D, launch velocity v_o, and other parameters, providing practicable measures for better retaining the viscous flow material volume. Therefore, many studies have proposed a dual-barrier system to investigate the upstream overflow behavior and downstream run-up impact mechanisms using physical modeling and numerical simulations [26,43,44]. In this study, 2D numerical flume tests were conducted using a SPH model to investigate the overflow behavior and impact mechanisms of a dual-barrier system with deflectors.

The setup of the 3D numerical flume models of the single barrier with deflectors and dual-barrier system are illustrated in Figs. 2a and 2b, and the detailed geometry of the 2D dual-barrier system with deflectors is shown in Fig. 2c. A rigid barrier with a 65-mm-long deflector (L_d) was placed 800 mm from the initial position of the viscous granular flow, and the height of the upstream barrier (B_u) was 100 mm. The downstream barrier (B_d) was sufficiently tall to intercept overflowing debris flow. The distance between the barriers (D_{ud}) is described in [43]. Initially, the viscous debris flow volume was set up (cross-section: 300 mm × 200 mm). The slope angle α was fixed to 26°. Various deflector angles were considered, based on the flume test described in a previous study [12]. More detailed information regarding the modeling scenarios, including various barrier heights and the distance between barriers are listed in Table 3. This study adopted a unit weight of 11.35 kN·m^{-3} for natural debris flow containing fine-grained pyroclastic soil in southern Italy, as estimated from *in-situ* experimental data [18]. Natural debris flows are a mixture of solid particles and viscous liquid [45]. High-density features always appear in high-mobility and large debris flow events [46]. In this study, the debris flow was modeled as a homogeneous non-Newtonian fluid using the Herschel–Bulkley model.

The Herschel–Bulkley (HB) model was used to model the debris flow. The HB model has been widely used to investigate the rheological behavior of natural debris flow [47,48]. The deviatoric viscous stress tensor τ is expressed as follows:

$$\begin{aligned} \tau &= \tau_y + K\dot{\gamma}^N \quad \text{if } \dot{\gamma} \neq 0 \\ \tau &\leq \tau_y \quad\quad\quad \text{otherwise,} \end{aligned} \tag{12}$$

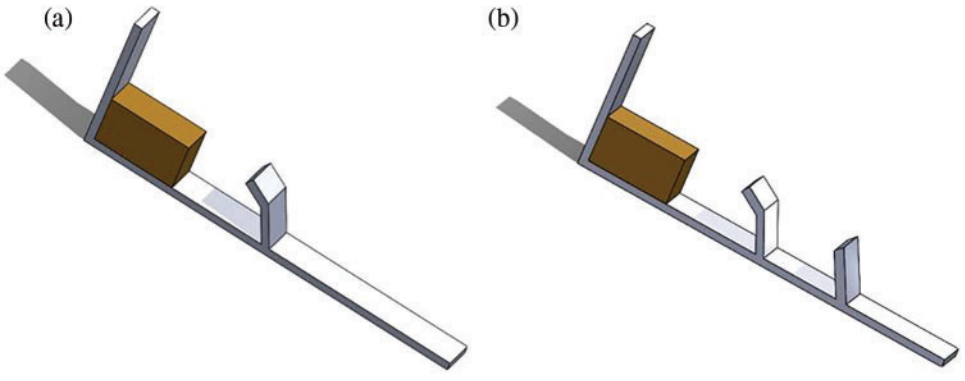

Figure 2: (Continued)

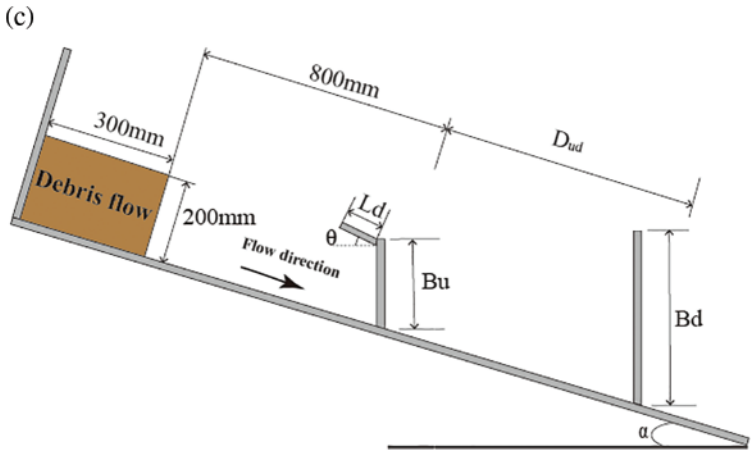

Figure 2: Numerical model setup: (a) 3D single barrier with deflectors; (b) 3D dual-barrier system; (c) 2D dual-barrier system with deflectors

In Eq. (12), $\tau_y = ptan\varphi + c$ is the yield stress used for landslide modeling [31]; φ and c are the frictional angle and cohesion, respectively. For viscous debris flow, τ_y is a modeling constant, K is the consistency index, and N is the power-law exponent. The rheological parameters used in the numerical modeling were obtained from experiments [18] and are listed in Table 1. Additionally, $\dot{\gamma}$ is the second invariant of the rate-of-strain tensor; $\boldsymbol{S}$ is the rate-of-strain tensor calculated by the velocity gradient $\nabla \boldsymbol{u}$ between particles, as follows:

$$\dot{\gamma} = (2\boldsymbol{S}\colon \boldsymbol{S})^{1/2}$$
$$\boldsymbol{S} = \frac{1}{2}(\nabla \boldsymbol{u} + (\nabla \boldsymbol{u})^T) \tag{13}$$

Table 1: Rheological parameters used in numerical modeling

Rheological properties	Parameters
$\rho\ (kg/m^3)$	1135
$\tau_y\ (N/m^2)$	90
$K\ (Pa \cdot s)$	4.526
N	0.795

The apparent viscosity η_{app} can be used to calculate the stress tensor $\boldsymbol{\tau}$, which is expressed as follows:

$$\boldsymbol{\tau} = 2\eta_{app}\boldsymbol{S}$$
$$\eta_{app} = \frac{\tau_y}{\dot{\gamma}} + K\dot{\gamma}^{N-1} \tag{14}$$

The above model is singular in the static state when $\dot{\gamma} = 0$. Therefore, this study used a cutoff shear rate of $\dot{\gamma}_{cutoff} = 0.1\ s^{-1}$ to prevent singular viscosity at zero shear rates [49]. Here, η_{cutoff} is the

cutoff viscosity when $\dot{\gamma} < \dot{\gamma}_{cutoff}$, as calculated by $\frac{\tau_y}{\dot{\gamma}_{cutoff}} + K\dot{\gamma}_{cutoff}^{N-1}$.

$$\eta_i = \begin{cases} \eta_{cutoff} & \text{if } \dot{\gamma} < \dot{\gamma}_{cutoff} \\ \eta_{app} & \text{if } \dot{\gamma} > \dot{\gamma}_{cutoff} \end{cases} \tag{15}$$

2.3 Model Validation

The dam break test reported by a previous study [50] was first used to calibrate the proposed numerical models. Fig. 3 shows the geometry of the dam break test and monitoring locations H1 and H4. Additionally, the physical and rheological parameters of the test fluid are listed in Table 2. As mentioned in the description of the rheological model in the Subsection 2.2, the debris flow viscosity is calculated by $\eta_{app} = \frac{\tau_y}{\dot{\gamma}} + K\dot{\gamma}^{N-1}$. When the power-law exponent $N = 1$ and yield stress $\tau_y = 0$, the HB model can be converted to the Bingham model.

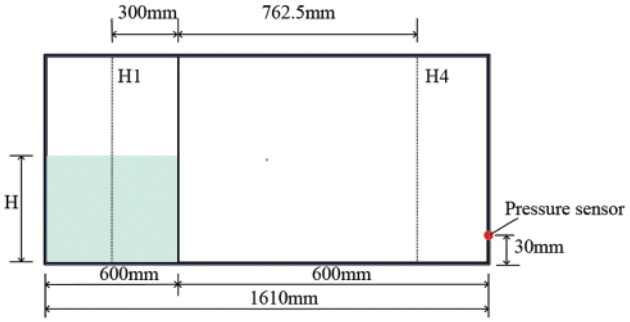

Figure 3: Dam break model test

Table 2: Physical and rheological parameters used in dam break test

Rheological properties	Parameters
ρ (kg/m^3)	997
τ_y (N/m^2)	0
K (Pa · s)	0.001
N	1
L; H (m)	0.6; 0.3 /0.6

The simulated results obtained by the proposed model were compared to the experimental results and are presented in Figs. 4 and 5. Fig. 4 mainly compares the relative flow elevation (h/H), which varied with non-dimensional time ($t^* = t\sqrt{g/H}$), of the numerical and experimental results; H represents the initial height of the dam break. Figs. 4a and 4b shows the temporal evolution of the flow levels at the given locations H1 and H4 for an initial height $H = 0.3$ m, which agrees well with the literature data, including the arrival of the primary wave at location H4. The relative load pressure ($P/\rho gH$) varied with the non-dimensional time t^*, and the pressure sensor was located at the right end of the box with a height of 0.03 mm to monitor the pressure variations. Fig. 5 shows that the impact pressure load was slightly higher than the experimental data when the initial height of the dam break was $H = 0.3$ m, and approximately the same when $H = 0.6$ m.

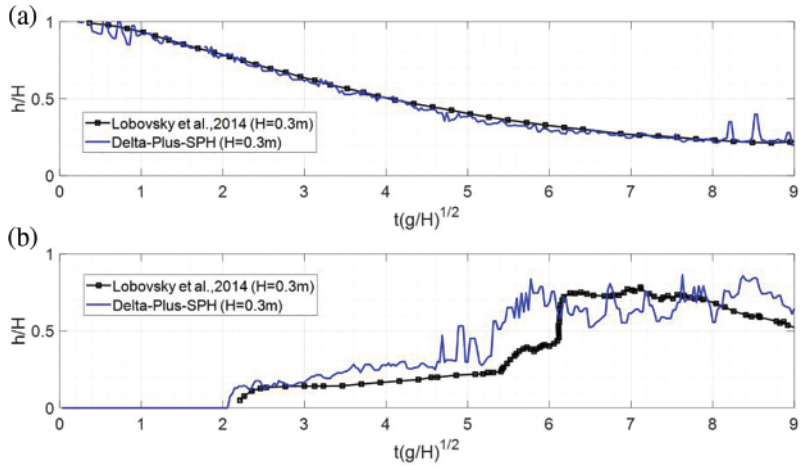

Figure 4: (a) Fluid level elevations at location H1 and (b) Fluid level elevations at location H4, compared with literature data [50]

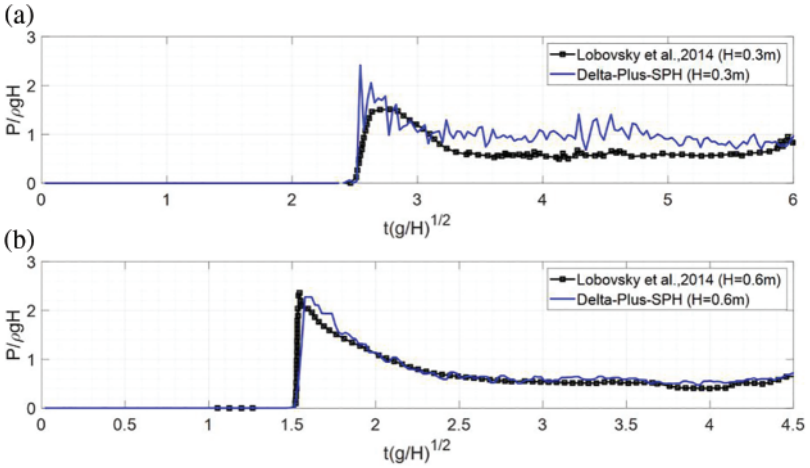

Figure 5: (a) $H = 0.3$ m: impact pressure from pressure sensor, and (b) $H = 0.6$ m: impact pressure from pressure sensor, compared with literature data [50]

3 Results and Discussion

Unlike water, when a viscous debris flow collides with an obstacle, the flow velocity decreases dramatically, leading to an approximately triangular zone of a fluid at rest forming upstream of the obstacle. This deposited zone is referred to as a "dead zone" in mudflow [51]. The ensuing flow mounts this dead zone and expends part of its energy before hitting the barrier [1,24,52]. When the barrier's retention capacity is reached, an overflow effect occurs: the debris flow material begins to escape from the barrier and flows forward through the barrier crest [53]. A dimensionless parameter $D_F = L_{DZ}/L_d$ is introduced to quantitatively analyze the dead-zone formation [54]; L_{DZ} is the length of the dead zone, and L_d is the deflector length. Throughout the fluid–structure interaction, the dead zone acts as a buffer layer, possibly aiding in the dissipation of the flow's kinetic energy and the redirection of its momentum [55]. Upon reaching the flume base, the viscous fluid exhibits a tendency to flow back, which is very different to the behavior of a dry granular material (Fig. 6).

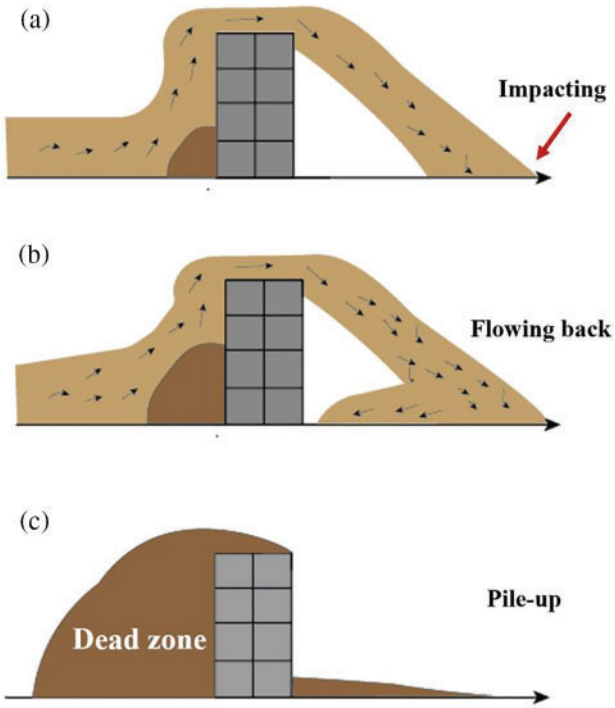

Figure 6: Schematic diagram of viscous debris overflow barrier (a) before and (b) after impact on flume base; (c) dead-zone formation

To gain a better understanding of the deflector's robustness against disasters, the kinetic energy E_K is introduced as a measure of the system's dynamic behavior, as follows:

$$E_K = \frac{1}{2}\sum_{i=1}^{N_p} m_i \left|\boldsymbol{u}_i\right|^2 \tag{16}$$

Here, N_p denotes the total number of fluid particles within the interaction domain in the monitored domain (ranging between $x = 1.05$ m and $x = 1.15$ m); the term m_i refers to the mass of particle i; $|\boldsymbol{u}_i|$ denotes the velocity magnitude of particle i. The retention efficiency (RE) of the barrier is used to quantify the proportion of the viscous flow particles retained by the upstream barrier [56]. In Eq. (17), $m_{retention}$ is the mass of viscous flow particles upstream of the barrier, and m_{total} is the total mass of the released viscous flow particles.

$$RE = \frac{m_{retention}}{m_{total}} \tag{17}$$

This study investigated the effect of single and dual-barrier systems with a deflector angle of 26° on viscous debris flow. To investigate the interaction between the viscous debris flow and the dual-barrier system, upstream and downstream barriers with different heights ($B/h = 2$–5), and the distance between the barriers, were simulated. Here, h represents the maximum flow depth in the open channel test. Detailed information is provided in Table 3.

At the upstream barrier position, the flow thickness and front flow velocity were measured in the open-channel test (H0-WD) to calculate $h_{max} = 0.042$ m (shown in Fig. 7).

Table 3: Numerical investigation scenarios

Test ID	Deflector angle (°)	Upstream barrier height (mm)	Distance between barriers	Downstream barrier height (mm)
H0-WD (Open-channel test)	No deflector	/	/	/
H10-WD1	No deflector	250	/	/
H10-WD2	No deflector	100	/	/
H10-D0	0	100	/	/
H10-D30	30	100	/	/
H10-D45	45	100	/	/
H10-D60	60	100	/	/
H10-D0-H25	0	100	700	250
H10-D30-H25	30	100	700	250
H10-D45-H25	45	100	700	250
H10-D60-H25	60	100	700	250
H10-WD1-H25	No deflector	100	700	250
H10-WD-H18	No deflector	100	700	180
H10-WD2-H25	No deflector	100	400	250
H18-WD-H25	No deflector	180	400	250

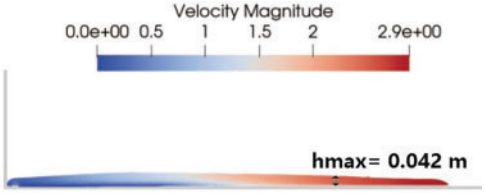

Figure 7: Open-channel test ($t = 0.625$ s)

Based on the simulation results, the rest of this paper focuses on the overflow pattern and pile-up mechanisms, and discusses the energy dissipation under the influence of the deflector angles, dead zone, and retention ability of the barrier with different barrier heights and location setups.

3.1 Overflow Pattern and Energy Dissipation

Fig. 8 illustrates the dynamic behavior of viscous flow overflow with and without deflectors. A single barrier with a height of 100 mm and deflector angles ranging from 0° to 60° was considered. Orthogonal deflectors (0°) and 30° deflectors caused the viscous flow to overflow the barrier quickly, resulting in higher velocity magnitude. The distance traveled by the overflow and its points of impact on the channel base are defined as the launch length (D); the flow launch angle is defined as the angle between the overflow direction and the horizontal line [12]. In this study, the viscous flow reached the

base of the slope (approximately $t = 1.05$ s) of each scenario to calibrate the launch angle and length for subsequent investigations.

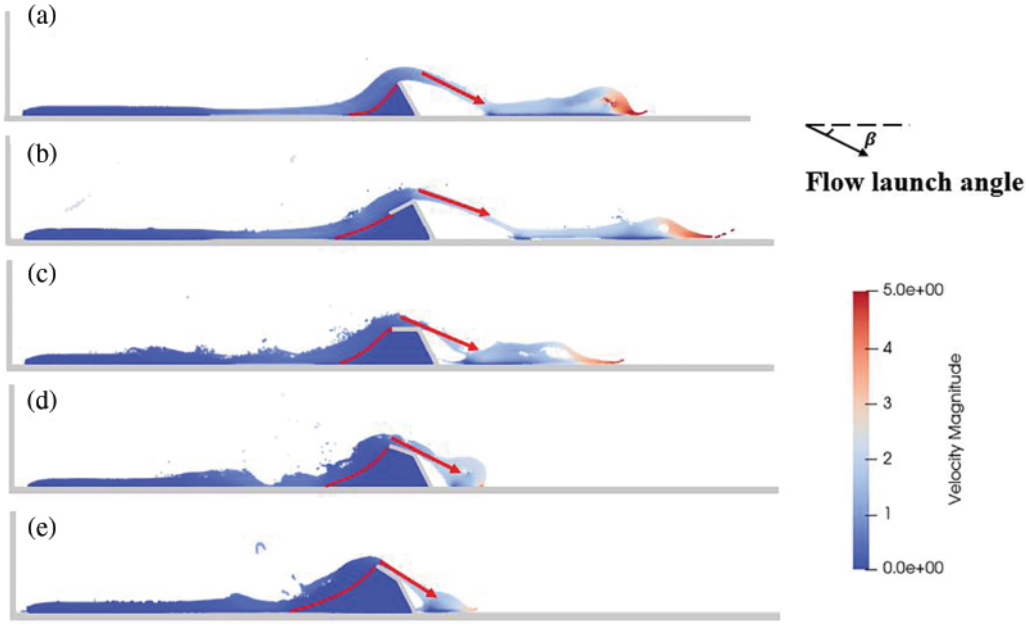

Figure 8: Overflow mechanisms: (a) without deflector (H10-WD2: $t = 1.05$ s); (b) deflector angle $\theta = 0°$ (H10-D0: orthogonal deflector, $t = 1.025$ s); (c) deflector angle $\theta = 30°$ (H10-D30: $t = 1.075$ s); (d) deflector angle $\theta = 45°$ (H10-D45: $t = 1.05$ s); (e) deflector angle $\theta = 60°$ (H60-D0: $t = 1.1$ s)

Deflectors with larger angles lead to a shorter launch length and larger launch angles when the viscous debris flow overflows the barrier and lands on the flume base. As shown in Fig. 9a, the launch length decreased from 1.845 to 1.273 m as the deflector angle increased from zero to 45°. However, the effect was less pronounced when the deflector angle exceeded 45°. The launch length of a barrier without deflectors (1.715 m) is marginally shorter compared with that of orthogonal deflectors (0°). The launch angle increased from approximately 20° to 35° as the deflector's angles (ranging from 0° to 60°) increased (Fig. 9b).

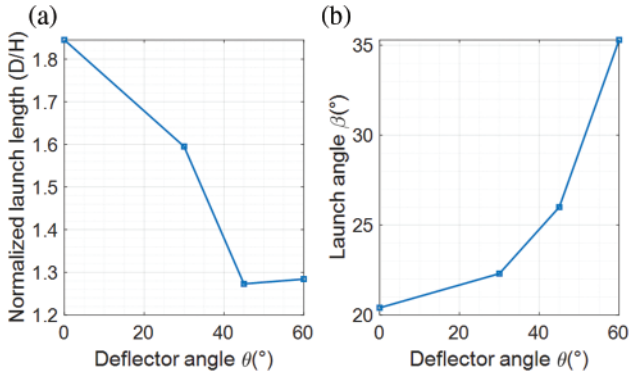

Figure 9: Influence of deflector angles on (a) launch length and (b) launch angle

In Fig. 10, the size of the dead-zone area markedly increases with the introduction of a barrier equipped with deflectors. Additionally, the dimensionless length of the dead-zone is positively correlated with the deflector angles. When the deflector angle exceeds 30°, the dimensionless length of the dead-zone increases significantly, reaching values above 3.5.

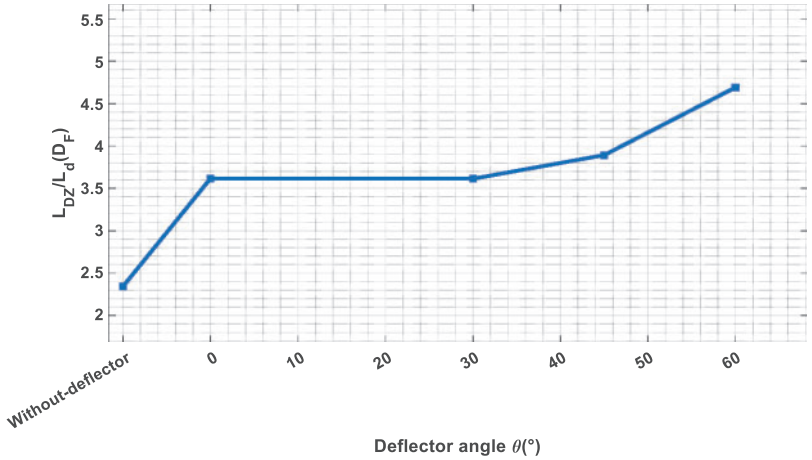

Figure 10: Influence of deflector angles on dimensionless length of dead-zone (D_F)

Fig. 11 illustrates the general evolution of overflow kinetic energy with various deflector angles, which can be categorized into three phases. Before impacting on the barrier, there is a kinetic energy peak in the process, owing to the acceleration of the debris flow. Phase 2 involves the dissipation process of the kinetic energy induced by the deflectors. Compared with barriers with deflectors, the kinetic energy of barriers without deflectors immediately increases, indicating a significant increase in the particle velocity. However, barriers with deflectors experience a period of zero kinetic energy when entering Phase 2 of dissipation, primarily because the deflectors directly intercept the impacting particles and then create a dead zone.

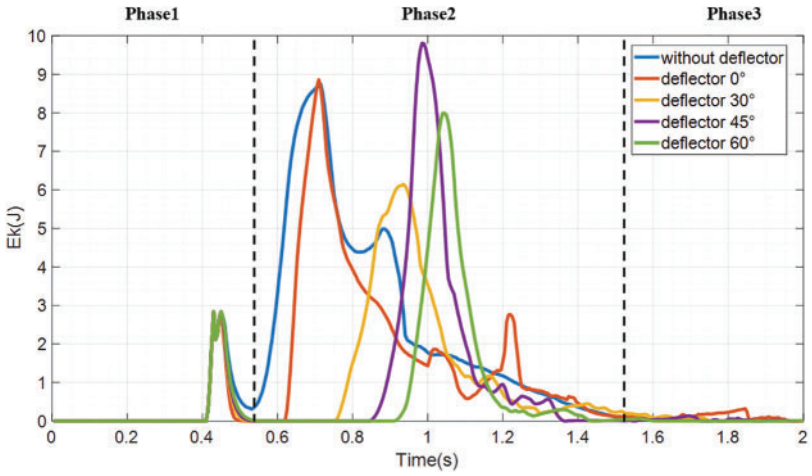

Figure 11: Evolution of overflow kinetic energy with different deflector angles

The overflow velocity magnitude and viscous debris direction are largely influenced by the deflector angles. The barrier with orthogonal deflectors exhibits a dissipation process similar to that of a barrier without a deflector, leading to the longest launch length. Although the 45° deflector significantly reduces the launch length, its capability of energy dissipation is inferior to that of the 60° and 30° deflectors within the monitored section. In the H10-D45 test program (Fig. 12), the dead zone starts to form when the flow impacts the barrier, and gradually grows and controls the overflow behavior observed around $t = 1$ s of the viscous flow after the flow–barrier interaction and dead-zone formation. The dead-zone characteristics are discussed below.

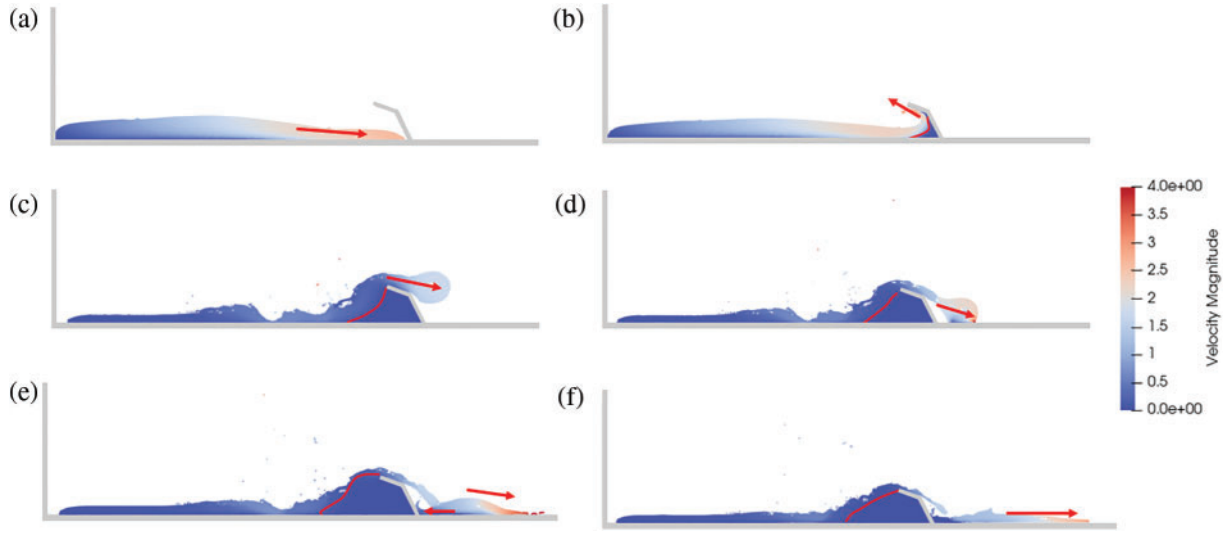

Figure 12: Flow–barrier interaction mechanisms under deflector angle $\theta = 45°$ (H10-D45): (a) $t = 0.425$ s; (b) $t = 0.475$ s; (c) $t = 1$ s; (d) $t = 1.05$ s; (e) $t = 1.1$ s; (f) $t = 1.5$ s

The energy dissipation of the dual-barrier system exhibits characteristics similar to the three stages observed in the single barrier structure described earlier (Fig. 13). The energy accumulation phase follows a pattern of initial increase and subsequent decrease. Compared with the upstream barrier with a height of 100 mm, the barrier with a height of 180 mm exhibits a zero-energy zone owing to the formation of a larger dead zone. The distance between barriers affects the energy dissipation process. A shorter distance results in a larger proportion of particles flowing back to the upstream barrier with higher velocity. In contrast, the downstream barrier with a height of 180 mm effectively intercepts the released viscous debris flow.

3.2 Pile-Up Mechanism and Retention Efficiency

The barrier height, barrier location, and deflector angles greatly influence the control of the dynamic behavior of viscous flow. As shown in Fig. 14, increasing the height of a single barrier from 100 mm ($B/h = 2.38$) to 250 mm ($B/h = 5.95$) leads to the complete retention of viscous debris flow and dead-zone formation.

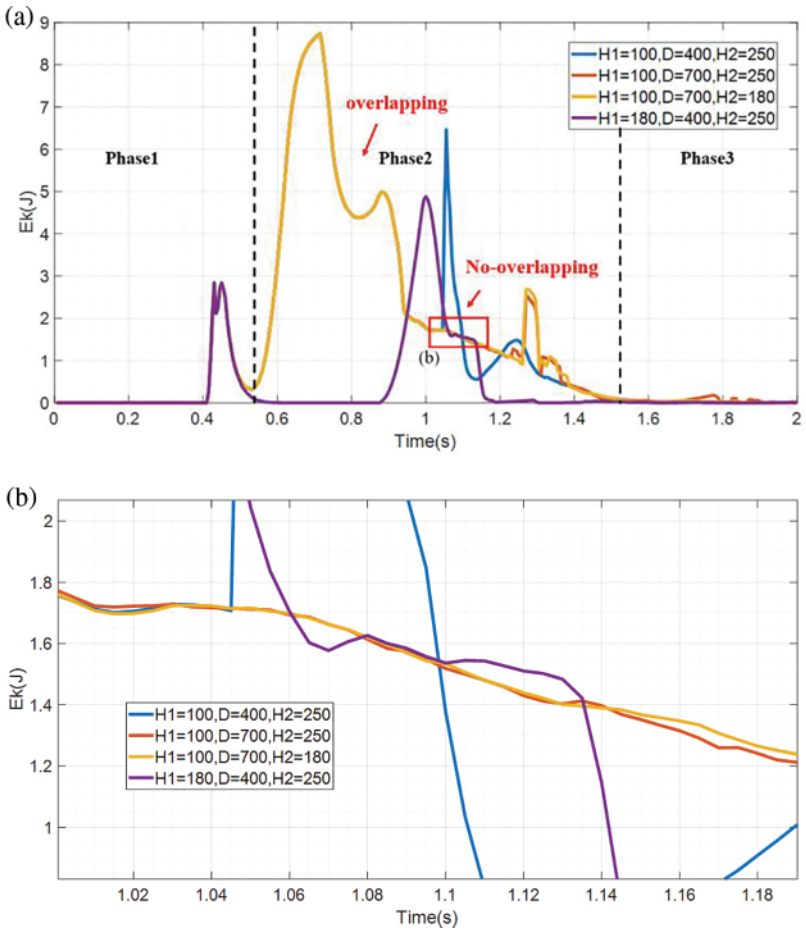

Figure 13: Evolution of overflow kinetic energy under different conditions of dual-barrier system: (a) global; (b) detail

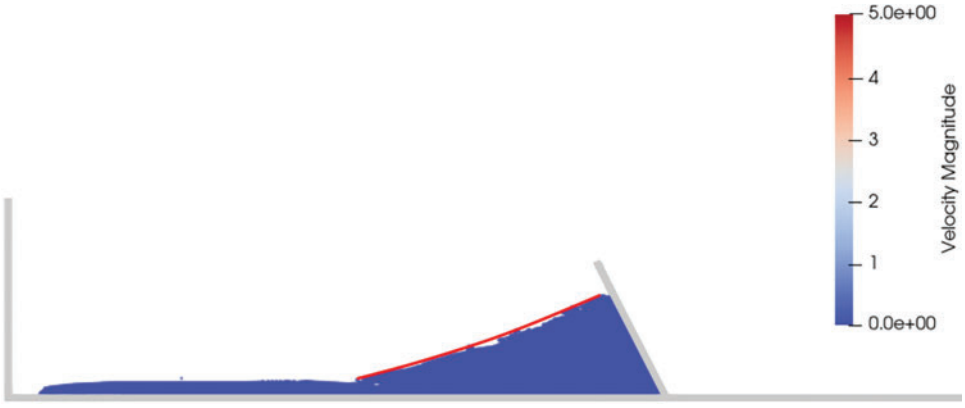

Figure 14: Pile-up mechanism of barrier with height of 250 mm (H10-WD1: $t = 3.45$ s)

In this study, barriers with heights of 100 and 180 mm were investigated at distances of 400 and 700 mm, respectively. When the upstream barrier was equipped with deflectors, a downstream barrier

height of 250 mm could intercept the entire debris volume in four test programs. The deflector angle influenced the formation of the dead zone near the deflectors, with larger angles resulting in more pronounced ramp-like dead zones. The results are presented in Fig. 15, illustrating that the dead zone serves as cushion layer at the upstream barrier. The impact of the overflowing debris flow on the downstream barrier results in the formation of dead zones with different sizes. Particularly, the upstream barrier equipped with an orthogonal deflector exhibits the highest momentum, leading to the rapid interception of viscous flow by the downstream barrier.

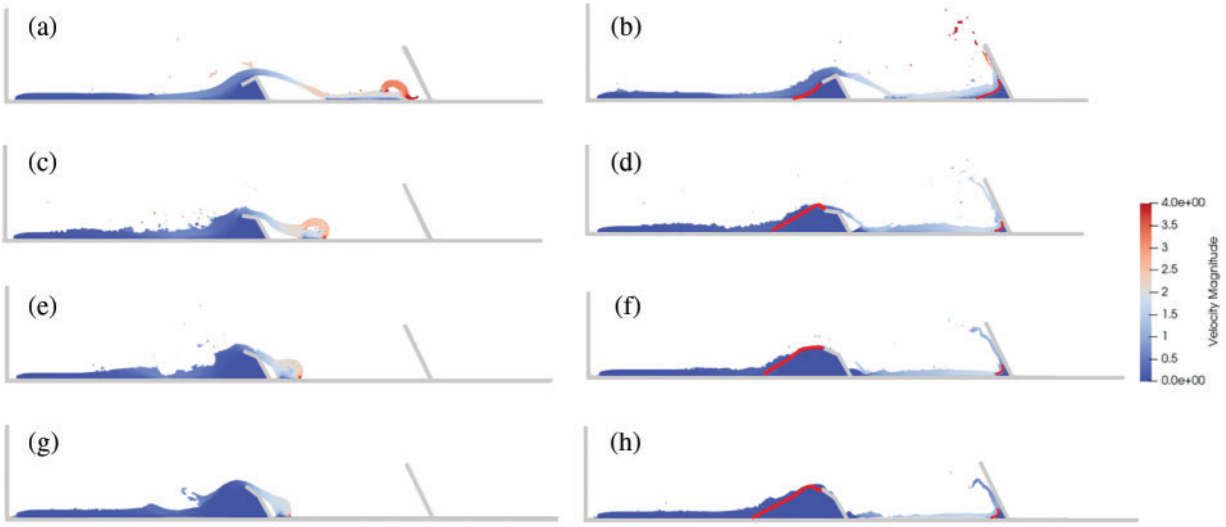

Figure 15: Pile-up mechanisms under influence of deflector angles: H10-D0-H25 (a) $t = 1$ s, (b) $t = 1.075$ s; H10-D30-H25: (c) $t = 1.025$ s, (d) $t = 1.25$ s; H10-D45-H25: (e) $t = 1.05$ s, (f) $t = 1.35$ s; H10-D60-H25: (g) $t = 1.075$ s, (h) $t = 1.45$ s

Larger deflector angles can effectively retain a larger amount of debris flow. Fig. 16 shows that the deflector's debris flow interception capability increases and then stabilizes starting from approximately 1.5 s. As shown in Fig. 17, when the deflector angle $\theta \geq 45°$, more than 80% of the released debris flow can be retained, indicating strong mitigation capability.

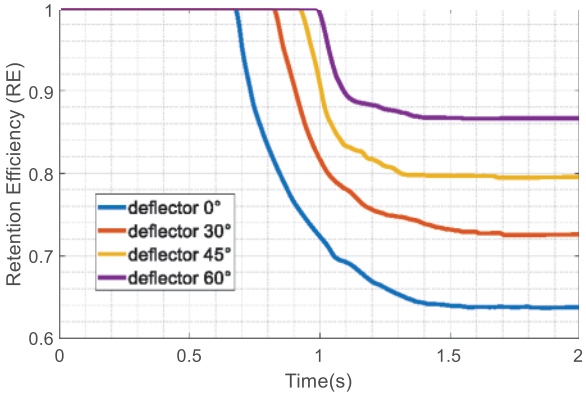

Figure 16: Time series of retention efficiency under influence of deflector angles

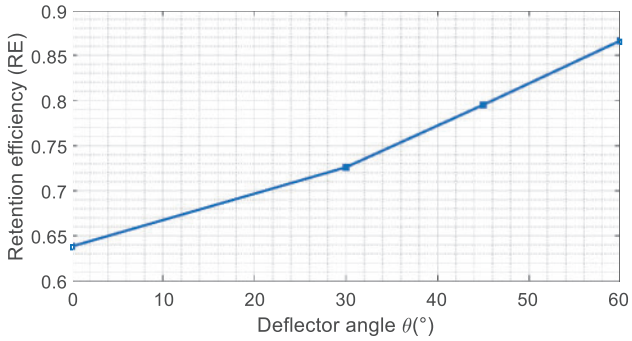

Figure 17: Influence of deflector angle on retention efficiency

In a dual-barrier system without deflectors, the ramp-like dead zones become steeper as the height of the upstream barrier increases (Fig. 18). Although the barrier distance is reduced by 42.9% to 300 mm, the downstream barrier retains the highest debris flow volume. Compared with the single barrier with retention efficiency (Fig. 19), the upstream barrier with a height of 180 mm intercepted over 90% of the debris flow, exceeding the interception of approximately 40% achieved by the upstream barrier with a height of 100 mm.

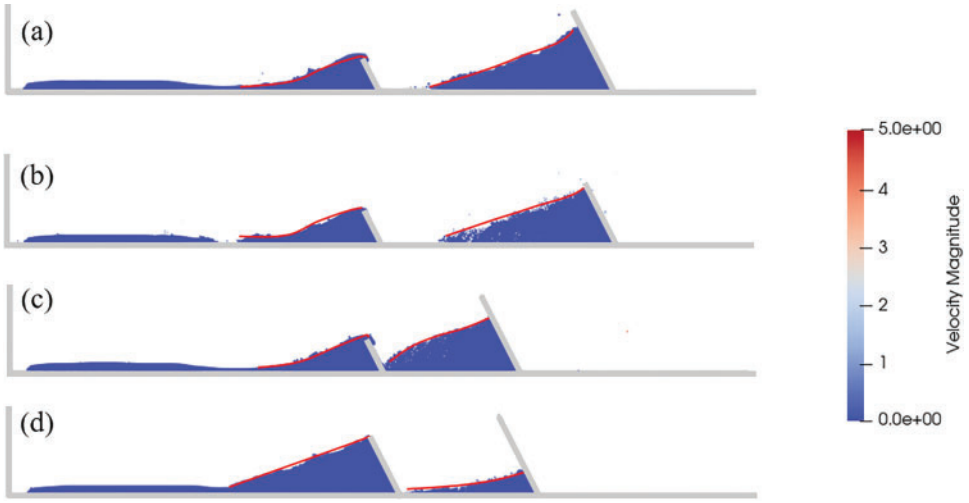

Figure 18: Pile-up mechanisms: (a) H10-WD-H25: $t = 2.34$ s; (b) H18-WD1-H25: $t = 3$ s; (c) H18-WD2-H25: $t = 3$ s; (d) H18-WD-H25: $t = 3$ s

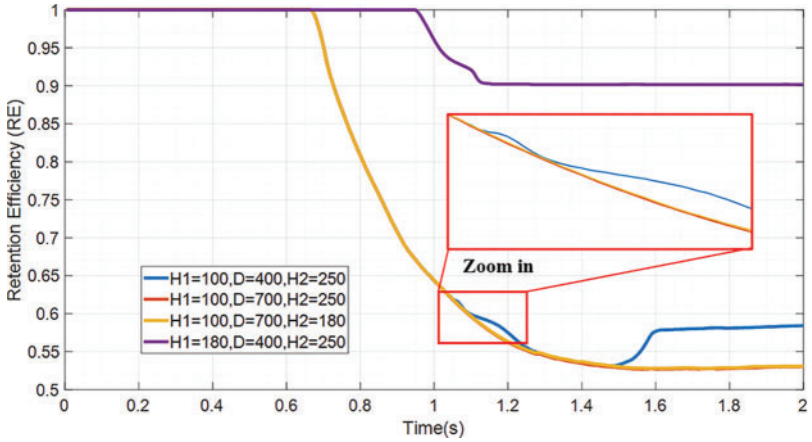

Figure 19: Time series of upstream barrier retention efficiency under different dual-barrier system conditions

4 Conclusion

This study investigated the interaction of viscous debris flow with barriers that have different deflector angles, and the impact of a dual-barrier system with different barrier heights and distances. The main conclusions are as follows:

(1) The interaction between viscous debris flows and barriers is largely determined by the deflector angles. Specifically, a deflector angle below 45° forms shallow ramp-like zones, promoting a thick and high-speed overflow downstream. The dimensionless length of the dead zone increases significantly when the deflector angle exceeds 30°. Moreover, the overflow mechanisms vary owing to the intricacies of viscous debris flows, with back-flows becoming more obvious when the flow velocity increases and the launch length decreases. There are three stages of energy in the dissipation process: the cumulative phase, interaction phase, and plateau phase.

(2) The barrier's height and downstream positioning profoundly influence the effectiveness of single barriers in retaining flows. For instance, a barrier height decreasing from 250 to 180 mm cuts the retained flow volume by approximately one tenth, while a height reduction to 100 mm decreases the volume by approximately 40%. In dual-barrier systems, the spacing between the barriers also affects the dead-zone formation.

Although this study provides insights into the role of deflectors and dual-barrier systems against debris flows, further research into other influencing factors and the three-dimensional effects during viscous debris flow–structure interactions is required.

Acknowledgement: The authors thank the editor and the reviewers for their help to improve the quality of our manuscript.

Funding Statement: This study was supported by the National Natural Science Foundation of China (Grant Nos. 42120104008 and 42207198).

Author Contributions: Conceptualization, Y.H. and D.F.; methodology, B.L. and H.S.; formal analysis, B.L. and H.S.; investigation, B.L.; writing—original draft preparation, B.L.; writing—review and editing, Y.H. and D.F.; visualization, B.L.; supervision, D.F.; funding acquisition, Y.H. and D.F. All authors have read and agreed to the published version of the manuscript.

Availability of Data and Materials: The data sets used and analysed during this study are available from the corresponding author upon reasonable request.

Conflicts of Interest: The authors declare that they have no conflicts of interest to report regarding the present study.

References

1. Koo, R. C. H., Kwan, J. S. H., Ng, C. W. W., Lam, C., Choi, C. E. et al. (2017). Velocity attenuation of debris flows and a new momentum-based load model for rigid barriers. *Landslides, 14(2),* 617–629.
2. Pan, H., Wang, R., Huang, J., Ou, G. (2013). Study on the ultimate depth of scour pit downstream of debris flow sabo dam based on the energy method. *Engineering Geology, 160,* 103–109.
3. Hungr, O., Leroueil, S., Picarelli, L. (2014). The Varnes classification of landslide types, an update. *Landslides, 11(2),* 167–194.
4. Ng, C. W. W., Choi, C. E., Goodwin, S. R., Cheung, W. W. (2017). Interaction between dry granular flow and deflectors. *Landslides, 14(4),* 1375–1387.
5. Schoonees, T. (2014). *Impermeable recurve seawalls to reduce wave overtopping (Ph.D. Thesis)*. Stellenbosch University.
6. Kortenhaus, A., Pearson, J., Bruce, T., Allsop, N. W. H., van der Meer, J. W. (2003). Influence of parapets and recurves on wave overtopping and wave loading of complex vertical walls. *Coastal Structures, 2003,* 369–381.
7. Verwaest, T., Vanpoucke, P., Willems, M., de Mulder, T. (2011). Waves overtopping a wide-crested dike. *Coastal Engineering Proceedings, 1(32)*.
8. Kwan, J. S. H. (2012). Supplementary technical guidance on design of rigid debris-resisting barriers. Geotechnical Engineering Office, HKSAR. *GEO Report*, 270.
9. Su, N., Xu, L., Yang, B., Li, Y., Gu, F. (2023). Risk assessment of single-gully debris flow based on dynamic changes in provenance in the wenchuan earthquake zone: A case study of the qipan gully. *Sustainability, 15(15),* 12098.
10. Kato, F., Suwa, Y., Watanabe, K., Hatogai, S. (2012). Mechanisms of coastal dike failure induced by the Great East Japan Earthquake Tsunami. *Coastal Engineering Proceedings, 1(33)*.
11. Castellino, M., Sammarco, P., Romano, A., Martinelli, L., Ruol, P. et al. (2018). Large impulsive forces on recurved parapets under non-breaking waves. A numerical study. *Coastal Engineering, 136,* 1–15.
12. Choi, C. E., Ng, C. W. W., Goodwin, S. R., Liu, L. H. D., Cheung, W. W. (2016). Flume investigation of the influence of rigid barrier deflector angle on dry granular overflow mechanisms. *Canadian Geotechnical Journal, 53(10),* 1751–1759.
13. Takahashi, T., Das, D. K. (2014). *Debris flow: Mechanics, prediction and countermeasures*, 2nd edition. UK: CRC Press.
14. Wang, T., Chen, X., Li, K., Chen, J., You, Y. (2018). Experimental study of viscous debris flow characteristics in drainage channel with oblique symmetrical sills. *Engineering Geology, 233,* 55–62.
15. Kong, Y., Zhao, J., Li, X. (2021). Hydrodynamic dead zone in multiphase geophysical flows impacting a rigid obstacle. *Powder Technology, 386,* 335–349.
16. Ng, C. W. W., Li, Z., Wang, Y. D., Liu, H., Poudyal, S. et al. (2023). Influence of deflector on the impact dynamics of debris flow against rigid barrier. *Engineering Geology, 321,* 107135.

17. Huang, X., García, M. H. (1998). A Herschel-Bulkley model for mud flow down a slope. *Journal of Fluid Mechanics, 374,* 305–333.
18. Schippa, L. (2020). Modeling the effect of sediment concentration on the flow-like behavior of natural debris flow. *International Journal of Sediment Research, 35(4),* 315–327.
19. Huang, Y., Jin, X., Ji, J. (2022). Effects of barrier stiffness on debris flow dynamic impact—II: Numerical simulation. *Water, 14(2),* 182.
20. Zanuttigh, B., Lamberti, A. (2007). Instability and surge development in debris flows. *Reviews of Geophysics, 45(3),* RG3006.
21. Coussot, P., Laigle, D., Arattano, M., Deganutti, A., Marchi, L. (1998). Direct determination of rheological characteristics of debris flow. *Journal of Hydraulic Engineering, 124(8),* 865–868.
22. Ren, Z., Zhao, X., Liu, H. (2019). Numerical study of the landslide tsunami in the South China Sea using Herschel-Bulkley rheological theory. *Physics of Fluids, 31(5),* 056601.
23. Shi, H., Huang, Y. (2022). A GPU-based δ-plus-SPH model for non-newtonian multiphase flows. *Water, 14(11),* 1734.
24. Zhang, B., Huang, Y. (2021). Unsteady overflow behavior of polydisperse granular flows against closed type barrier. *Engineering Geology, 280,* 105959.
25. Li, X., Zhao, J. (2018). A unified CFD-DEM approach for modeling of debris flow impacts on flexible barriers. *International Journal for Numerical and Analytical Methods in Geomechanics, 42(14),* 1643–1670.
26. Vicari, H., Tran, Q. A., Nordal, S., Thakur, V. (2022). MPM modelling of debris flow entrainment and interaction with an upstream flexible barrier. *Landslides, 19(9),* 2101–2115.
27. Bui, H. H., Sako, K., Fukagawa, R., Wells, J. (2008). SPH-based numerical simulations for large deformation of geomaterial considering soil-structure interaction. *The 12th International Conference of International Association for Computer Methods and Advances in Geomechanics (IACMAG)*, pp. 570–578. Goa, India.
28. Bui, H. H., Nguyen, G. D. (2021). Smoothed particle hydrodynamics (SPH) and its applications in geomechanics: From solid fracture to granular behaviour and multiphase flows in porous media. *Computers and Geotechnics, 138,* 104315.
29. Fan, X. J., Tanner, R. I., Zheng, R. (2010). Smoothed particle hydrodynamics simulation of non-Newtonian moulding flow. *Journal of Non-Newtonian Fluid Mechanics, 165(5),* 219–226.
30. Wang, W., Chen, G., Han, Z., Zhou, S., Zhang, H. et al. (2016). 3D numerical simulation of debris-flow motion using SPH method incorporating non-Newtonian fluid behavior. *Natural Hazards, 81(3),* 1981–1998.
31. Dai, Z., Huang, Y., Cheng, H., Xu, Q. (2017). SPH model for fluid-structure interaction and its application to debris flow impact estimation. *Landslides, 14(3),* 917–928.
32. Sun, P. N., Colagrossi, A., Marrone, S., Antuono, M., Zhang, A. M. (2019). A consistent approach to particle shifting in the δ-Plus-SPH model. *Computer Methods in Applied Mechanics and Engineering, 348,* 912–934.
33. Sun, P. N., Le Touzé, D., Oger, G., Zhang, AM. (2021). An accurate FSI-SPH modeling of challenging fluid-structure interaction problems in two and three dimensions. *Ocean Engineering, 221,* 108552.
34. Laigle, D., Lachamp, P., Naaim, M. (2007). SPH-based numerical investigation of mudflow and other complex fluid flow interactions with structures. *Computational Geosciences, 11(4),* 297–306.
35. Liu, G. R., Liu, M. B. (2003). *Smoothed particle hydrodynamics: A meshfree particle method*. Singapore: World Scientific.
36. Wendland, H. (1995). Piecewise polynomial, positive definite and compactly supported radial functions of minimal degree. *Advances in Computational Mathematics, 4(1),* 389–396.
37. Lind, S. J., Xu, R., Stansby, P. K., Rogers, B. D. (2012). Incompressible smoothed particle hydrodynamics for free-surface flows: A generalised diffusion-based algorithm for stability and validations for impulsive flows and propagating waves. *Journal of Computational Physics, 231(4),* 1499–1523.

38. Yang, L., Rakhsha, M., Hu, W., Negrut, D. (2022). A consistent multiphase flow model with a generalized particle shifting scheme resolved via incompressible SPH. *Journal of Computational Physics, 458,* 111079.
39. Antuono, M., Marrone, S., di Mascio, A., Colagrossi, A. (2021). Smoothed particle hydrodynamics method from a large eddy simulation perspective. Generalization to a quasi-Lagrangian model. *Physics of Fluids, 33(1),* 015102.
40. Hu, X. Y., Adams, N. A. (2007). An incompressible multi-phase SPH method. *Journal of Computational Physics, 227(1),* 264–278.
41. Sun, P. N., Colagrossi, A., Marrone, S., Zhang, A. M. (2017). The δplus-SPH model: Simple procedures for a further improvement of the SPH scheme. *Computer Methods in Applied Mechanics and Engineering, 315,* 25–49.
42. Adami, S., Hu, X. Y., Adams, N. A. (2012). A generalized wall boundary condition for smoothed particle hydrodynamics. *Journal of Computational Physics, 231(21),* 7057–7075.
43. Ng, C. W. W., Choi, C. E., Koo, R. C. H., Goodwin, S. R., Song, D. et al. (2018). Dry granular flow interaction with dual-barrier systems. *Géotechnique, 68(5),* 386–399.
44. Zhang, B., Huang, Y. (2022). Effect of unsteady flow dynamics on the impact of monodisperse and bidisperse granular flow. *Bulletin of Engineering Geology and the Environment, 81(2),* 77.
45. Kong, Y., Li, X., Zhao, J., Guan, M. (2023). Load–deflection of flexible ring-net barrier in resisting debris flows. In: *Géotechnique*, pp. 1–13. https://doi.org/10.1680/jgeot.22.00135
46. Li, Y., Liu, J., Su, F., Xie, J., Wang, B. (2015). Relationship between grain composition and debris flow characteristics: A case study of the Jiangjia Gully in China. *Landslides, 12(1),* 19–28.
47. Guo, T., Zhao, K., Zhang, Z., Gao, X., Qi, X. (2017). Rheology study on low-sugar apple jam by a new nonlinear regression method of Herschel-Bulkley model. *Journal of Food Processing and Preservation, 41(2),* e12810.
48. Kang, D. H., Hong, M., Jeong, S. (2021). A simplified depth-averaged debris flow model with Herschel-Bulkley rheology for tracking density evolution: A finite volume formulation. *Bulletin of Engineering Geology and the Environment, 80(7),* 5331–5346.
49. Shi, H., Huang, Y., Feng, D. (2022). Numerical investigation on the role of check dams with bottom outlets in debris flow mobility by 2D SPH. *Scientific Reports, 12(1),* 20456.
50. Lobovský, L., Botia-Vera, E., Castellana, F., Mas-Soler, J., Souto-Iglesias, A. (2014). Experimental investigation of dynamic pressure loads during dam break. *Journal of Fluids and Structures, 48,* 407–434.
51. Kong, Y., Guan, M., Li, X., Zhao, J., Yan, H. (2022). How flexible, slit and rigid barriers mitigate two-phase geophysical mass flows: A numerical appraisal. *Journal of Geophysical Research: Earth Surface, 127(6),* e2021JF006587.
52. Song, D., Zhou, G. G. D., Xu, M., Choi, C. E., Li, S. et al. (2019). Quantitative analysis of debris-flow flexible barrier capacity from momentum and energy perspectives. *Engineering Geology, 251,* 81–92.
53. Ren, M., Shu, X. (2020). A novel approach for the numerical simulation of fluid-structure interaction problems in the presence of debris. *Fluid Dynamics & Materials Processing, 16(5),* 979–991. https://doi.org/10.32604/fdmp.2020.09563
54. Laigle, D., Labbe, M. (2017). SPH-based numerical study of the impact of mudflows on obstacles. *International Journal of Erosion Control Engineering, 10(1),* 56–66.
55. Faug, T., Lachamp, P., Naaim, M. (2002). Experimental investigation on steady granular flows interacting with an obstacle down an inclined channel: Study of the dead zone upstream from the obstacle. Application to interaction between dense snow avalanches and defence structures. *Natural Hazards and Earth System Sciences, 3(4),* 187–191.
56. Shen, W., Luo, G., Zhao, X. (2022). On the impact of dry granular flow against a rigid barrier with basal clearance via discrete element method. *Landslides, 19(2),* 479–489.